MM Science Journal | www.mmscience.eu
ISSN 1803-1269 (Print) | ISSN 1805-0476 (On-line)
Special Issue | HSM 2025
18th International Conference on High Speed Machining
October 15-16, 2025, Metz, France
DOI: 10.17973/MMSJ.2025_12_2025167

HSM2025-45026

SIMULATION OF 5-AXIS MILLING SURFACE MORPHOLOGY USING BALL NOSE CUTTER

A. Rahmani[1,2*], J. Qian[1,2], S. Castagne[1,2]
[1]KU Leuven, Department of Mechanical Engineering, Leuven, Belgium
[2]Flanders Make@KU Leuven, Leuven, Belgium
*Corresponding author; e-mail: amirsajjad.rahmani@kuleuven.be

Abstract
The prediction of milled surface morphology in CAM software typically overlooks the interactions between the workpiece and tool, resulting in an approximate prediction of surface morphology. This study intends to enhance the prediction accuracy by simulating the actual cutting edge motion in 5-axis ball-end milling to overcome the limitations for applications requiring accurate surface morphology prediction. The CAM data generated by commercial software is processed first, and a detailed geometrical model for ball-nose cutting edges is developed. Then, the trochoidal motion of the cutting edges is simulated. Finally, a structured grid is used to represent the final machined surface.

Keywords:
5-axis milling, CAM, CLSF data, Surface morphology

1 INTRODUCTION

Surface morphology is one of the essential characteristics defining critical functional behaviors of manufactured parts. For instance, some of the main functional properties, such as microcontact behavior, frictional performance, wear resistance, and lubrication performance of manufactured products, are directly influenced by their surface morphology. In the context of multi-axis machining, CAM software is used to generate the tool path, providing useful outputs related to the geometry of the component. However, it remains challenging to provide a precise estimation of the generated surface pattern under different cutting parameters. This problem lies in the fact that most commercial CAM platforms tend to consider a conceptual engineering approach and ignore the actual phenomena occurring in the tool and workpiece interaction. These systems model the tool as a pure cylinder with a hemispherical dome at the top, neglecting the actual tool geometry and the effect of the cutting edges. This oversimplification can result in significant discrepancies between the predicted surface and manufactured surface features. It is especially remarkable in the feed direction, where the predicted scallop heights and cusp marks do not match closely with reality [Varga 2022]. As a result, manufacturers often resort to costly trial-and-error methods to ascertain the influence of machining parameters to obtain the desired surface qualities [Kaneko 2023].

There are several categories of models for predicting surface morphology, including empirical, analytical/numerical, simulation-based, semi-empirical, and AI-based. While empirical models can be very accurate under tested conditions, they have little applicability beyond the tested machining parameter range. Moreover, while analytical models are fast and accurate, they become tedious when dealing with complex manufacturing variations, such as vibrations. Simulation methods can effectively model material removal and machining variations (such as tool runout and deflection), which can be incorporated relatively easily in these approaches but demand substantial computing resources due to the discretization of the cutting tool and workpiece. Semi-empirical methods blend simulation with looking at empirical data to bridge between theoretical statistical insight and simulation models. However, modeling machining variations as statistical parameters can hamper the model's accuracy under varying machining conditions. In addition, artificial intelligence (AI) approaches give us strong pattern recognition but with very weak physical interpretability [Denkena 2021; Zhang 2018].

For semi-empirical models, Denkena et al. conducted a combined kinematic simulation (deterministic) and stochastic modeling by predicting the idealized surface topography based on IFW CutS software. To isolate stochastic elements, they aligned and compared profiles and then characterized their statistical distribution. This joint model enhanced the accuracy of the predictions [Denkena 2015, 2021]. The approach depends on having existing data from previous milling operations performed under identical processing parameters (e.g., series production) [Marin 2024].

In surface topography simulation, both the temporal resolution and the spatial refinement given to metal cutting simulation have a big impact on the accuracy of simulated results [Xiao 2023]. The simulation efficiency decreases proportionally when these parameters are considered at finer scales. To overcome these bottlenecks, Xiao et al.

presented an enhanced Z-MAP method based on the Sequential Quadratic Programming (SQP) algorithm to circumvent the high-level discretization of the cutting edges while maintaining comparable simulation precision with reduced computation costs. As for analytical models, Arizmendi et al. developed a model predicting ball-end milled surface topography that accounts for tool parallel axis offset [Arizmendi 2008]. The approach uses Chebyshev expansions to transform trajectory and envelope equations into solvable polynomial form, with confirmed accuracy by experimental validation. Dong et al. developed a novel analytical model for the 3D surface topography and roughness prediction of 5-axis CNC milling [Dong 2023]. Surface morphology was simulated by calculating the scallop endpoints without discretizing the workpiece, and the approach was validated through experiments. Although it is efficient, its reliance on scallop boundary calculations may not be possible when extending the model cases where the tool is positioned perpendicular to the surface, and the configuration would affect the mathematical definition of scallop formation used in this approach. Wang et al. developed a simulation model for thin-walled parts by incorporating the effects of cutting vibrations [Wang 2019]. They found that larger vibration amplitudes occur at sections with low stiffness, and feed mark patterns were generated on the machined surface with texture intervals approximately three times the feed per tooth. Similarly, in a study conducted by Batista et al., material ploughing was identified at the cutter center at very low cutting speeds, causing higher roughness due to more difficult tool engagement [Batista 2017].

Layegh et al. [Layegh 2017] developed a simulation model to predict surface topography in 5-axis ball-end milling by deriving trochoidal cutting edge motion with feed rate, tool inclination, and runout. For every plane perpendicular to the feed direction, they formed the 2-D convex hull of the intersection points to reconstruct the envelope. The study additionally demonstrated that the 3D surface roughness parameters (Sa and Sq) tend to rise when the lead angle, tilt angle, or their combination increases. In contrast, Xu et al. [Xu 2018] reported that the surface roughness decreases steeply with a tilt angle smaller than 6°. The roughness maintains constant, stable values for angles greater than this threshold. Furthermore, according to [Pesice 2023], for different tool diameters, there is a minimum angle limit threshold where the cutting speed is not high enough, and mostly ploughing happens instead of cutting, and after that critical angle, the roughness stabilizes. The contrast may be explained by the fact that where the radial runout is negligible, increasing the lead or tilt angle can generally lower the surface roughness, and this value becomes stable after a threshold where the effective cutting speed exceeds the minimum speed for cutting instead of ploughing. However, where the radial runout offset is significant, the runout effects become strong enough to degrade the surface [Marin 2024].

The existing models still overlook a few important factors in the machining process, including the true effect of cutting edge behavior, besides the integration of CAM data in real industrial cases. Consequently, the research explores the potential of using CAM data to investigate the influence of machining parameters on the morphology of the machined surface in 5-axis ball-end milling.

2 MATERIALS AND METHODS

2.1 CAM data and preprocessing data

A Cutter Location Source File (CLSF) was first generated using Siemens NX 2312 CAM software after the machining operation was programmed. Then, the cutter locations, tool orientations, and cutting and non-cutting moves (as a label) were extracted. An automated data-cleaning process was also implemented. The final dataset consists of seven columns: the first three columns, x, y, and z, which represent the tooltip positions in 3D space; and the next three columns $(\hat{\imath}, \hat{\jmath}, \hat{k})$, are the tool orientation vectors, and then the last column describes the cutting moves from non-cutting moves to prevent extra calculations in non-cutting move regions.

Fig. 1 (a) illustrates the cutter and workpiece in the Siemens CAM environment, Fig. 1 (b) shows Siemens NX 2312 simulation results with no scallops in the feed direction, and Fig. 1 (c) illustrates the tooltip positions after CLSF data cleaning.

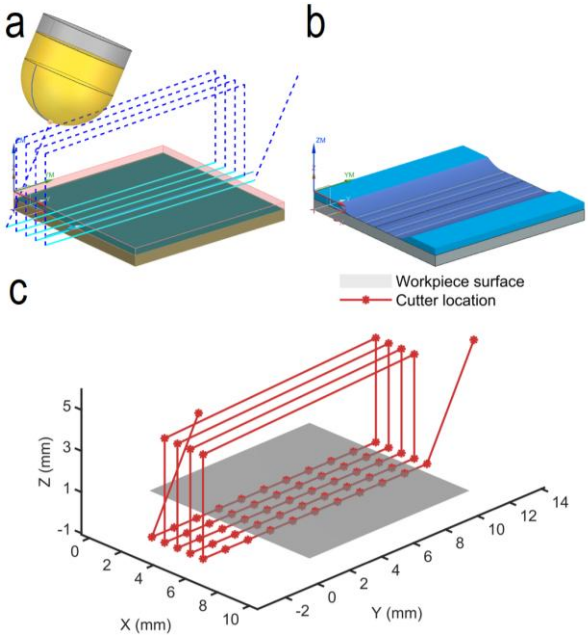

Fig. 1: Three-dimensional CAM simulation: (a) cutter and workpiece; (b) scallop-free Siemens NX CAM simulation; (c) tooltip positions and workpiece surface

2.2 Modeling of helical cutting edge geometry

The ball nose was modeled to depict the tool cutting edge in three dimensions in the Cartesian coordinate system, using a numerical modeling technique as described in the literature [Marin 2024] and https://www.geogebra.org/m/hkdr6rhj. The following equations (1) to (5) are reproduced to define the coordinates for every single point along the cutting edge:

$$\begin{cases} x_i = R\sin(\kappa_i)\sin(\theta_i), \\ y_i = R\sin(\kappa_i)\cos(\theta_i), \\ z_i = R - R\cos(\kappa_i), \end{cases} \quad (1)$$

where κ_i denotes the immersion angle for each point, ranging from 0 to $\pi/2$ (Fig. 2).

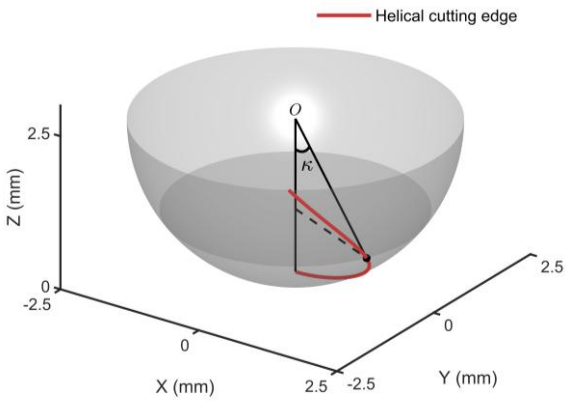

Fig. 2: Illustration of the geometry of the cutting edge

The parameter θ_i, which represents the angular position of these points on the cutting edge, and it is calculated as:

$$\theta_i = \varphi_0 - \varphi_i \tag{2}$$

Here, the initial angular position, φ_0, is defined as the angle measured from the positive x-axis and is determined by dividing a full circle (2π radians) into equal segments according to the number of cutting edges. The corresponding angles for a tool with two teeth are 0 and π radians. The angular increment, φ_i, is defined such that if the tool removes material in a clockwise direction, φ_i is assigned a negative value, and vice versa. To define θ_i along the cutting edges, a relationship derived from the helix geometry is employed as a function of the tool's height (Fig. 3).

$$tan(\alpha) \;=\; \frac{R\,\Delta\varphi}{\Delta z} \tag{3}$$

For each point along the cutting edge, the following expression is obtained:

$$tan(\alpha_i) \;=\; \frac{R_i\,\varphi_i}{z_i}, \tag{4}$$

where α (or α_i locally) is the helix angle of the tool, R (or R_i) is the radial distance at that point, and Δz is the incremental change in height.

By considering $z_i = R_i(1-\cos(\kappa_i))$, the angular increment φ_i is expressed as:

$$\varphi_i \;=\; (1-\cos(\kappa_i))\,\tan(\alpha). \tag{5}$$

By applying this formulation, the rotation around the tool axis ($R\,\Delta\varphi$) is consistently related to the vertical displacement Δz through the chosen helix angle α.

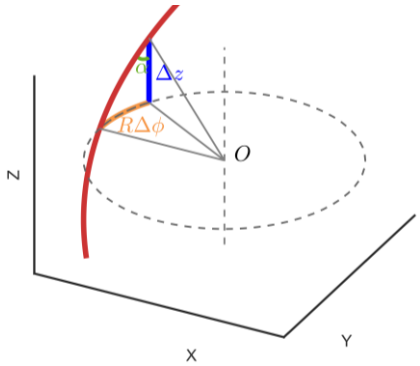

Fig. 3: Geometric relationships defining angular increment (φ_i) as a function of tool height.

2.3 Toolpath discretization and trochoidal motion of the cutting edges

After the preprocessing of the CAM data from Siemens NX, some sequential steps were developed to model the kinematics of ball-end milling tools in 5-axis machining. Accordingly, the toolpath positions and orientations are uniformly interpolated along the cumulative trajectory distance of each machining path (cutting moves) so that the resolution of the spacing is small enough to capture the rotation of points considered on the cutting edges. Between each new interpolated CL point, the time increment $\Delta t\ (s)$ is computed based on the linear distance increment $\Delta d\ (mm)$, the feed per tooth $f_z\ (mm/tooth)$, the number of teeth, and the angular velocity $\omega\ (rad/s)$:

$$\Delta t\ (\mathrm{s}) = \frac{\Delta d \times 2\pi}{f_z \times numTeeth \times \omega} \tag{6}$$

Subsequently, the constant rotation of the points on the cutting edges is simulated by computing the angular displacement: $\theta_{sim} = \omega \times t_i$. Although this calculation captures the rotational aspect, the full trochoidal motion results from the combination of simultaneous rotation and linear displacement of feed translation. Thus, a rigid body transformation is executed at each cutter location in two steps. The first step is to multiply the local tool coordinates (points on the cutting edge) by a rotation matrix (obtained using the Rodrigues rotation formula), which converts the local tool coordinates of the cutter to the global coordinates. In the second step, these discretized points on the cutting edge are translated into the global reference frame at each cutter location. Consequently, these transformations can accurately describe the rotational kinematics and the feed movement, whereby mapping the local coordinates to the global coordinates while reconstructing the trochoidal movement of cutting edges. This way, a three-dimensional swept volume of the cutter is generated (see Fig. 4 (a) and (b)), which can be further used to predict the resulting surface morphology. The trochoidal tool path simulation creates a uniform spacing equal to the feed-per-tooth value. The outermost part of these rotations creates the final surface morphology, demonstrating the engagement of cutting edges during the machining process (Fig. 4 (c)). Each edge produces a distinct surface texture mark at intervals, corresponding to f_z for a two-flute ball-nose cutter. This interval increases as the f_z increases. The next step is to find an accurate way to subtract the envelopes of the cutting edges from the workpiece surface to obtain the final surface morphology.

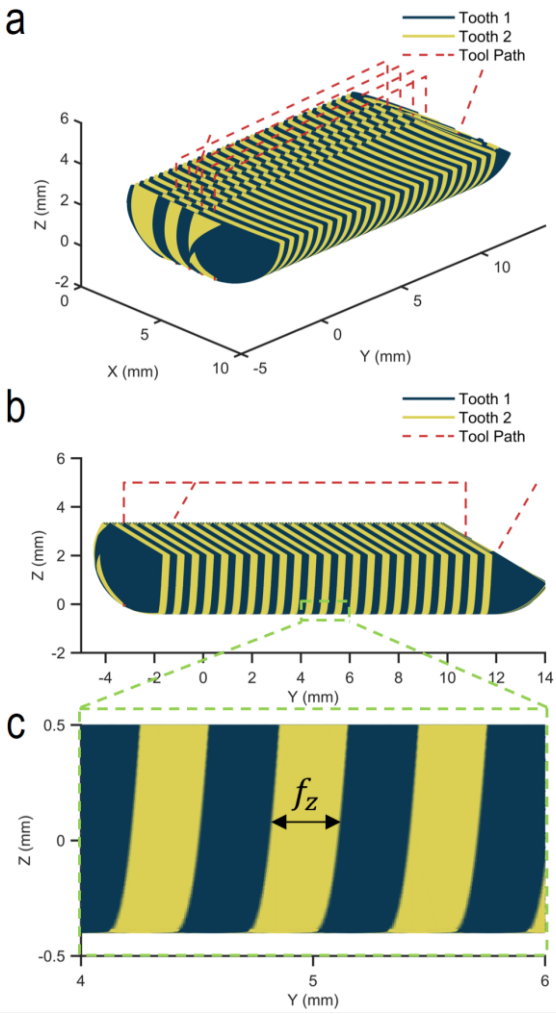

Fig. 4: Trochoidal movement of the cutting edges; (a) isometric view, (b) side view, and (c) magnified view of the feed per tooth (f_z= 0.3 mm/tooth) interval between consecutive cutting edges at the outermost part of the trochoidal movement.

2.4 Evaluating the surface topography

The three-dimensional trajectories of the cutting edge need to be converted into a height map to predict the machined surface topography from the trochoidal tool path data. It is insufficient to use the minimum value only to obtain the final surface morphology, since it will create an incomplete surface with missing features between sample points. Therefore, in addition to updating the grid points with the points of the cutting edges between two consecutive cutter locations, an interpolation of the points between these two is also necessary to update the height map.

The minimum and maximum of the X and Y coordinates of the trochoidal data were determined first to establish the machining mesh boundaries. Subsequently, a regular grid representing the tool swept region was generated at the required resolution, giving each grid point an initial Z-value of infinity to create meshes in 3D. These infinity values serve as reference points that will be replaced by actual heights wherever the cutting trajectories cross them. For every cutting tooth and each point along the cutting tooth, the associated trajectory is taken out and broken down into linear segments. They connect successive points of the cutter locations in the trochoidal movement.

To efficiently process these segments, rectangular bounding boxes have been built surrounding each linear segment, using a similar approach as described in reference [Liu 2024] and [Dong 2021]. For this localized region, the algorithm determines all the grid points that would potentially be affected by the cutting process by calculating the closest point distance from each grid node to the line segment and filtering only those grid points within a threshold distance (i.e., grid resolution divided by $\sqrt{2}$). They represent the maximum distance for a grid point marked as "cut" by the tool path. The value of this threshold is equal to half of the cell diagonal distance between the grid points, and this ensures that the tool path is covered even if it crosses the grid points at an angle.

A parameter value t, with a value of 0 at the start of a segment and a value of 1 at its end, has been applied for each grid point within a threshold distance, in order to find its relative position on the segment. The value of this parameter is calculated by projecting the point onto the line segment, clamped to the [0,1] range to allow interpolation between endpoints. With this parameter, the Z-values for each grid point can be calculated by linearly interpolating between the Z-values at the endpoints of a segment. If this interpolated Z-value is lower than the existing value, the grid point will replace it, thus ensuring that all grids retain the minimum Z-value and represent the deepest cut at that position (Fig. 5).

In order to create a point cloud that accurately depicts the finished machined surface and captures the microscale features created by the trochoidal tool paths, grid points with finite Z-values are extracted after processing all segments for all teeth, while discarding those still at infinity (representing unmachined areas).

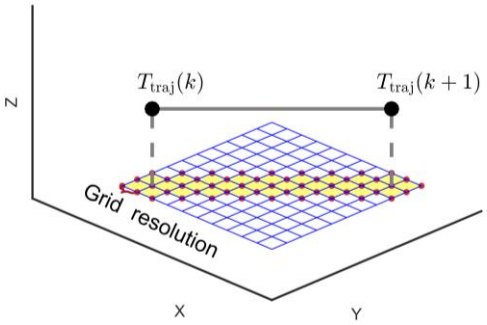

Fig. 5: Time-based discretization of tool trajectory into a small linear segment with highlighted grid points undergoing Z-value interpolation.

For visualization only on the workpiece aligned uniform grid, the tool swept cavity (computed minimum height samples) is resampled by assigning the minimum of the nominal workpiece surface height and the minimum cavity sample height in a small neighborhood around each node; if none is present, the node retains the nominal workpiece height. The displayed surface is the pointwise minimum of this resampled field and the nominal workpiece surface.

It should be noted that the overall simulation accuracy depends on the cutting edge discretization, workpiece grid resolution, and interpolation of cutter locations extracted from CAM software. In this research, each cutting edge consists of 3000 points. For the interpolation between cutter locations, linear interpolation with a uniform step size, equal to one-hundredth of the programmed f_z, is applied. This ensures evenly spaced cutter positions and smoothly varying tool axis orientations along the entire toolpath. Lastly, as for the workpiece resolution, on both X and Y axes, a grid resolution of 1 μm has been used on the workpiece surface.

3 RESULTS AND DISCUSSION

The simulations were carried out using the machining parameters as shown in Tab. 1, and the results for surface morphology are shown in Fig. 6 (a) and (b), respectively. Two surface patterns are produced in the scenarios of using spherical end mills perpendicular to each other, including scallops, which are determined by the feed per tooth (f_z) and cusps, which are determined by cutting width (a_e), as explained in the literature [Batista 2017]. The simulation results from Fig. 6 (a) and (b) are in accordance with these definitions.

Tab. 1: Machining parameters.

Process parameters	Value
Feed/tooth f_z (mm/tooth)	0.3
Spindle speed ω (rpm)	14000
Depth of cut a_p (mm)	0.4
Step over a_e (mm)	0.8
Tool diameter (mm)	5
Lead angle (degree°)	30
Tilt angle (degree°)	0
Number of teeth $numTeeth$	2

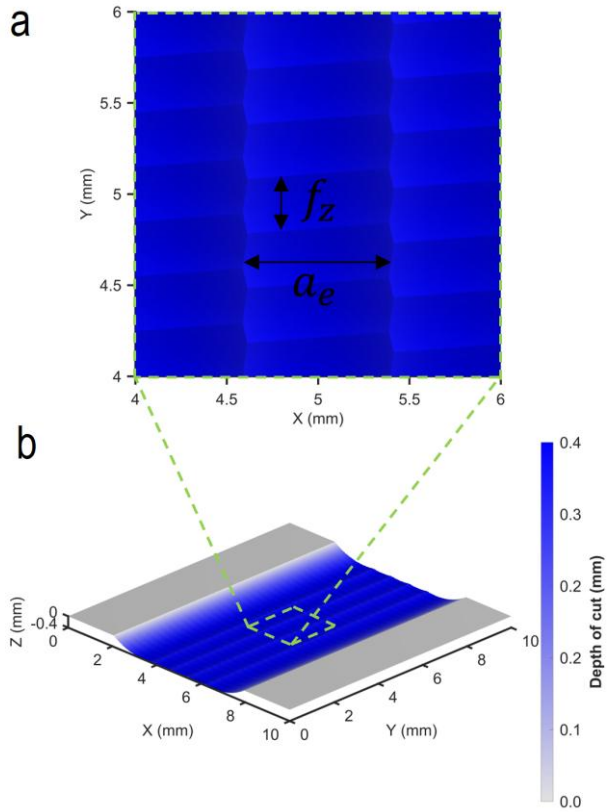

Fig. 6: Comparison of surface morphology: (a) magnified view of simulated surface texture, (b) complete machined surface simulation (lead angle: 30°, step over: 0.8 mm, f_z: 0.3 mm/tooth, depth of cut: 0.4 mm).

3.1 Validation against the literature

The validation of this research refers to the reported results by [Shujuan 2019]. A ball nose end mill (diameter 10 mm, two teeth) was used in the study, with a feed per tooth of f_z = 0.2 mm/tooth, a_e = 0.5 mm, a_p = 0.5 mm, ω = 3000 rpm, and tilt angle of 0°. The initial tooth phase was set to zero at the start of each pass. The lead angle was varied from 0° to 35° in 5° increments. The tool edge was discretized with 4000 points to maintain sufficiently tight spacing for the larger effective diameter, and a 1 μm workpiece grid was used. This discretization ensured stable contact detection and reduced aliasing because finer sampling captures smaller features. Agreement with the literature has been observed in two ways. First, the trend of maximum surface height versus lead angle closely matches the published curve across 0° – 35°, capturing the relatively larger maximum surface height at zero lead angle and the subsequent reduction toward a stable value (Fig. 7 (a)). The maximum height decreases from 7.5 μm at 0° (Fig. 7 (b)) to 6.8 μm at 5°. Beyond 10°, the values are stabilized to 7.2 μm at the lead angle of 35° (Fig. 7 (c)). This pattern is consistent with the contact moving off from the tool tip, raising local tangential speed and suppressing ploughing; beyond about 5° – 6°, the texture converges to a similar pattern.

Second, at a 30° lead angle and with the same aforementioned machining parameters, overlaying the section profiles in both feed and cross-feed directions reproduces the reported peak locations and amplitudes in (Fig. 8 (a,b)) [Shujuan 2019]. As for Ra, a straight line has been fitted to each cross-sectional profile with unweighted least squares. The arithmetic mean roughness is computed as the mean absolute deviation of the residual profile over the full span according to equation (7), and the results are reported in Tab. 2. Cross-feed roughness from the simulation matches closely with the experimental measurement. On the contrary, the feed direction roughness shows a noticeably larger deviation. The small discrepancy in the cross-feed direction is consistent with the hypothesis that the kinematic roughness is governed primarily by a_e and tool diameter. However, in the feed direction an underprediction (≈40% low) is expected because the roughness is governed by much smaller cusp heights and is therefore more sensitive to unmodeled effects (e.g., minimum chip thickness, elastic recovery, structural dynamics, and metrology errors). These outcomes indicate that the simulation reproduces both the trend and the magnitude of the published topography under similar cutting conditions.

$$R_a = \frac{1}{N}\sum_{i=1}^{N} |\, r_i - \bar{r}\,|, \quad \text{where} \quad \begin{cases} r_i = z_i - (\hat{a}\, x_i + \hat{b}), \\ \bar{r} = \frac{1}{N}\sum_{i=1}^{N} r_i . \end{cases} \tag{7}$$

Tab. 2: The Ra value in the feed and cross-feed directions

Ra (μm)			
Direction	**Experiment** [Shujuan 2019]	**Simulation**	**Error**
Feed direction	0.42	0.25	40.48%
Cross-feed direction	1.62	1.58	2.47%

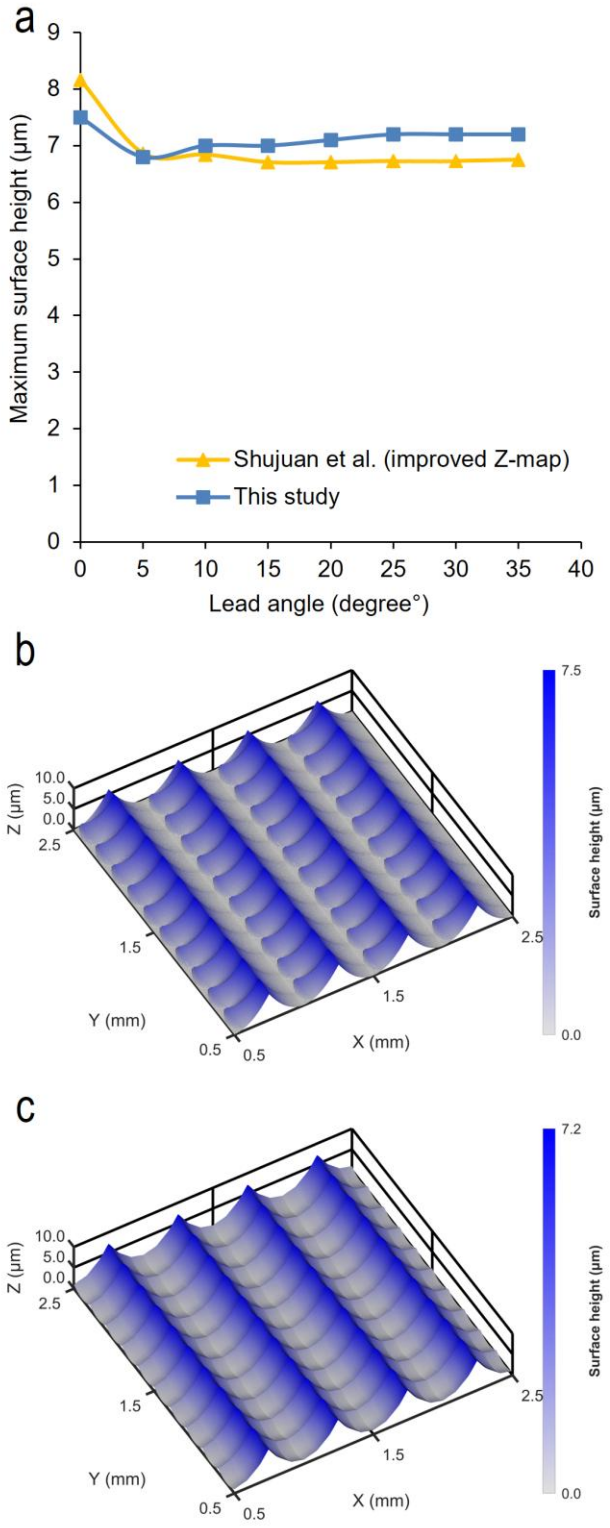

Fig. 7: (a) Maximum surface height versus lead angle: this study compared with [Shujuan 2019], (b,c) Simulated surface topographies at 0° and 35° lead angles, respectively

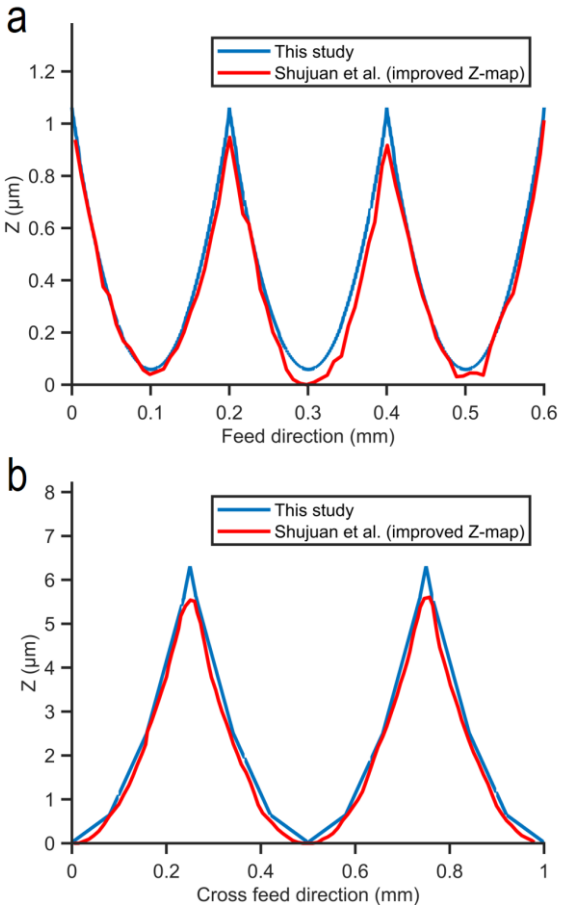

Fig. 8: (a) feed and (b) cross-feed line profiles comparing this study with [Shujuan 2019]

3.2 Computational cost and discretization

The computational cost of the simulation primarily depends on both the resolution of the discretization and the size of the workpiece. It can be approximated as $O(N_{CL} \cdot numTeeth \cdot M + G(h))$, where N_{CL} is the number of interpolated cutter locations, $numTeeth$ is the number of teeth (cutting edges), M is the number of points per cutting edge, and $G(h)$ is the total number of grid-cell update attempts. An increase in workpiece size or tooth count will lead to a rapid increase in computational costs. On our 16-core CPU (32 GB RAM), at a lead angle varied from 0° to 35° and with M = 4000 and h = 1 µm, the average total computation time is 432 seconds, including plotting. Increasing the N_{CL} beyond the baseline of $f_z/100$ will negligibly change the maximum surface height (100 nm), but dramatically increase computation time due to memory overhead. Increasing M beyond 4000 for a 10 mm cutter has little influence. But reducing M will produce missed grid updates and (visible spikes). A relation relating cutter diameter to M likely exists (e.g. $M \propto D/h$). The value used in this simulation was selected manually, and the grid resolution was set to h = 1 µm to ensure stable contact detection and reduce aliasing. As a practical guideline, a high resolution is recommended for fine finishing, and a coarser resolution is recommended for roughing.

4 CONCLUSIONS

This investigation has applied a simulation approach for predicting the surface morphology in milling with a ball nose tool. The following conclusions can be drawn from this exploratory research:

1. A simulation model has been developed to represent the topography of the machined surface in milling with a ball-end tool.
2. The use of CLSF data directly in the model gives interesting potential for further integration with existing CAM software to provide more reliable surface quality prediction without machining experiments.
3. It is demonstrated that introducing a lead angle smaller than ~ 5° is sufficient to eliminate the adverse cutting effects at the tool tip and achieve stable and low surface heights. Beyond this threshold, further increases in lead angle do not provide meaningful improvements in surface quality.
4. The model can predict surface morphology under the applied conditions and constraints. Cross-feed roughness agrees well with reported experiments in literature (2.47% error), whereas feed direction roughness turns out to be underpredicted (40.48% low), reflecting sensitivity to parameters missing in the model.

Future research will further optimize the model to improve its computational efficiency and take into account more manufacturing variables such as tool runout, vibration, and tool deflection.

5 ACKNOWLEDGEMENTS

This research work was financed and carried out within the framework of the Flanders Make SBO project "ROLUX".

6 DECLARATIONS

Declaration of use of Generative AI: GitHub Copilot Pro was used to assist with coding. After using this tool, the authors thoroughly reviewed and edited all content as needed and take full responsibility for the content of the publication.

Conflict of Interest: The authors declare that there is no conflict of interest.

7 REFERENCES

[Arizmendi 2008] M. Arizmendi, J. Fernández, L.N.L.D. Lacalle, A. Lamikiz, A. Gil, J.A. Sánchez, F.J. Campa, F. Veiga: Model development for the prediction of surface topography generated by ball-end mills taking into account the tool parallel axis offset. Experimental validation.CIRP Annals, 2008, Vol.57, No.1, pp 101–104. ISSN 00078506

[Batista 2017] M.F. Batista, A.R. Rodrigues, R.T. Coelho: Modelling and characterisation of roughness of moulds produced by high-speed machining with ball-nose end mill.Proceedings of the Institution of Mechanical Engineers, Part B: Journal of Engineering Manufacture, May 2017, Vol.231, No.6, pp 933–944. ISSN 0954-4054, 2041-2975

[Denkena 2015] B. Denkena, V. Böß, D. Nespor, P. Gilge, S. Hohenstein, J. Seume: Prediction of the 3D Surface Topography after Ball End Milling and its Influence on Aerodynamics.Procedia CIRP, 2015, Vol.31, pp 221–227. ISSN 22128271

[Denkena 2021] B. Denkena, M.-A. Dittrich, J. Huuk: Simulation-based surface roughness modelling in end milling.Procedia CIRP, 2021, Vol.99, pp 151–156. ISSN 22128271

[Dong 2023] J. Dong, Z. Chang, J. He, S. Liu, N. Wan: A novel simulation model of three-dimensional surface topography for five-axis CNC milling using bull-nose tool.The International Journal of Advanced Manufacturing Technology, October 2023, Vol.128, No.11–12, pp 5041–5060. ISSN 0268-3768, 1433-3015

[Dong 2021] Y. Dong, S. Li, Q. Zhang, P. Li, Z. Jia, Y. Li: Modeling and Analysis of Micro Surface Topography from Ball-End Milling in a Trochoidal Milling Mode.Micromachines, September 2021, Vol.12, No.10, pp 1203. ISSN 2072-666X

[Kaneko 2023] K. Kaneko, M. Inui, I. Nishida: Fast simulation of machining error induced by elastic deformation of tool system in end milling. 2023.

[Layegh K 2017] S.E. Layegh K, I. Lazoglu: 3D surface topography analysis in 5-axis ball-end milling.CIRP Annals, 2017, Vol.66, No.1, pp 133–136. ISSN 00078506

[Liu 2024] J. Liu, Y. Niu, Y. Zhao, L. Zhang, Y. Zhao: Prediction of Surface Topography in Robotic Ball-End Milling Considering Tool Vibration.Actuators, February 2024, Vol.13, No.2, pp 72. ISSN 2076-0825

[Marin 2024] F. Marin, A. Fagali De Souza, H. Da Silva Gaspar, A. Calleja-Ochoa, L.N. López De Lacalle: Topography simulation of free-form surface ball-end milling through partial discretization of linearised toolpaths.Engineering Science and Technology, an International Journal, July 2024, Vol.55, pp 101757. ISSN 22150986

[Pesice 2023] M. Pesice, P. Vavruska, J. Falta, P. Zeman, J. Maly: Identifying the lead angle limit to achieve required surface roughness in ball-end milling.The International Journal of Advanced Manufacturing Technology, April 2023, Vol.125, No.7–8, pp 3825–3838. ISSN 0268-3768, 1433-3015

[Shujuan 2019] L. Shujuan, Y. Dong, Y. Li, P. Li, Z. Yang, R.G. Landers: Geometrical simulation and analysis of ball-end milling surface topography.The International Journal of Advanced Manufacturing Technology, June 2019, Vol.102, No.5–8, pp 1885–1900. ISSN 0268-3768, 1433-3015

[Varga 2022] J. Varga, E. Spišák, I. Gajdoš, P. Mulidrán: Comparison of Milling Strategies in the Production of Shaped Surfaces.Advances in Science and Technology Research Journal, December 2022, Vol.16, No.6, pp 267–274. ISSN 2080-4075, 2299-8624

[Wang 2019] Z. Wang, B. Wang, J. Yuan: Modeling of surface topography based on cutting vibration in ball-end milling of thin-walled parts.The International Journal of Advanced Manufacturing Technology, April 2019, Vol.101, No.5–8, pp 1837–1854. ISSN 0268-3768, 1433-3015

[Xiao 2023] Y. Xiao, G. Ge, Z. Zeng, X. Feng, Z. Du: An improved Z-MAP method based on the SQP algorithm for fast surface topography simulation of ball-end milling.The International Journal of Advanced Manufacturing Technology, September 2023, Vol.128, No.3–4, pp 1863–1878. ISSN 0268-3768, 1433-3015

[Xu 2018] J. Xu, H. Zhang, Y. Sun: Swept surface-based approach to simulating surface topography in ball-end CNC milling.The International Journal of Advanced Manufacturing Technology, September 2018, Vol.98, No.1–4, pp 107–118. ISSN 0268-3768, 1433-3015

[Zhang 2018] Q. Zhang, S. Zhang, W. Shi: Modeling of surface topography based on relationship between feed per tooth and radial depth of cut in ball-end milling of AISI H13 steel.The International Journal of Advanced Manufacturing Technology, April 2018, Vol.95, No.9–12, pp 4199–4209. ISSN 0268-3768, 1433-3015